RESEARCH

Open Access

Photonic-chip-based dense entanglement distribution

Shang-Yu Ren[1,2†], Wei-Qiang Wang[3,4†], Yu-Jie Cheng[1,2], Long Huang[3,4], Bing-Zheng Du[3], Wei Zhao[3,4], Guang-Can Guo[1,2,5], Lan-Tian Feng[1,2*], Wen-Fu Zhang[3,4*] and Xi-Feng Ren[1,2,5*]

†Shang-Yu Ren and Wei-Qiang Wang contributed equally to this work.

*Correspondence:
fenglt@ustc.edu.cn;
wfuzhang@opt.ac.cn; renxf@ustc.edu.cn

[1] CAS Key Laboratory of Quantum Information, University of Science and Technology of China, Hefei 230026, China
[2] CAS Center for Excellence in Quantum Information and Quantum Physics, University of Science and Technology of China, Hefei 230026, China
[3] State Key Laboratory of Transient Optics and Photonics, Xi'an Institute of Optics and Precision Mechanics, Chinese Academy of Sciences, Xi'an 710119, China
[4] University of Chinese Academy of Sciences, Beijing 100049, China
[5] Hefei National Laboratory, University of Science and Technology of China, Hefei 230088, China

Abstract

The dense quantum entanglement distribution is the basis for practical quantum communication, quantum networks and distributed quantum computation. To make entanglement distribution processes stable enough for practical and large-scale applications, it is necessary to perform them with the integrated pattern. Here, we first integrate a dense wavelength-division demultiplexing system and unbalanced Mach-Zehnder interferometers on one large-scale photonic chip and demonstrate the multi-channel wavelength multiplexing entanglement distribution among distributed photonic chips. Specifically, we use one chip as a sender to produce high-performance and wideband quantum photon pairs, which are then sent to two receiver chips through 1-km standard optical fibers. The receiver chip includes a dense wavelength-division demultiplexing system and unbalanced Mach-Zehnder interferometers and realizes multi-wavelength-channel energy-time entanglement generation and analysis. High quantum interference visibilities prove the effectiveness of the multi-chip system. Our work paves the way for practical entanglement-based quantum key distribution and quantum networks.

Introduction

Multi-user entanglement distribution and analysis at different locations are practical requirements for quantum networks and distributed quantum computation. The systems often involve numerous independent building blocks, such as beam splitters (BSs), modulators and delay lines [1, 2], which always need a large space and bear mechanical and thermal disturbances [3, 4]. Compared to free-space optics and fiber optics, photonic integrated circuits (PICs) are promising platforms to overcome these difficulties due to their small footprint, scalability, programmability, and stability [5–9]. PICs provide opportunities to demonstrate large-scale quantum information processing that contains numerous optical components with millimeter scale, that is, quantum photonic integrated circuits (QPICs) [10, 11]. For example, multidimensional quantum entanglement [12], quantum teleportation [13] and various quantum algorithms [14–17] have been demonstrated on QPICs.

In quantum networks, to enhance the transmission capacity, make full use of wideband entangled photons [18–21] and increase the number of users, dense wavelength-division

multiplexing (DWDM) techniques are often used for quantum communication and play a key role in many quantum network architectures [1, 22, 23]. Besides, compared to polarization and frequency entanglement, entanglement with time basis is insensitive to polarization and frequency dispersion in fiber transmission and can be maintained in fiber networks, and thus is widely used. For example, combining unbalanced Mach-Zehnder interferometers (UMZIs) with DWDM components, energy-time entanglement states are used for long-distance quantum entanglement distribution among multiple users [24–26]. To improve the compactness and practicability of the system, key components need to be integrated monolithically. In fact, we have seen many attempts in recent years. For example, UMZIs are integrated on the silicon nitride (SiN) platform to generate time bins and analyze entanglement [27, 28]. As a main choice for integrated DWDM systems [29], arrayed waveguide gratings (AWGs) have been integrated on silica [30, 31], silicon-on-insulator (SOI) [32–34], SiN [35], thin-film lithium niobate on insulator (LNOI) [36] and polymer platforms [37]. However, these works are subject to limited scale, and in particular, the two most critical components—DWDMs and UMZIs have not been completely integrated on one single chip.

In this work, we realize the integration of a 32-channel high-performance AWG and 32 UMZIs on a single chip based on a high-index doped silica (HIDS) platform for large-scale quantum networks. Furthermore, we achieve the multi-wavelength energy-time entanglement distribution among three chips. As shown in Fig. 1, one fiber-packaged silicon nanowire works as the sender to generate wideband quantum photon pairs, and the other two receivers are integrated on the HIDS platform for the preparation and analysis of the energy-time entanglement. On the receiver chips, multiple wavelength channels support simultaneous operations by different users. Even if the chips are separated with
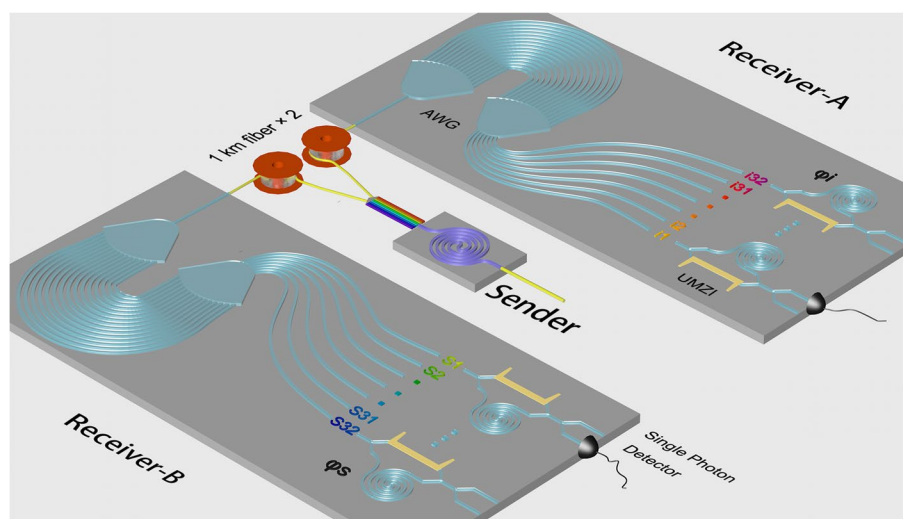

Fig. 1 Schematic diagram of multi-chip interconnection for energy-time entanglement distribution. The silicon-on-insulator chip is the sender and generates correlated wideband photon pairs via the spontaneous four-wave mixing process. The photons are divided and sent to two receivers of the quantum network. At the receiver terminal, photons are subdivided into different wavelength channels by the AWG. Entanglement preparation and analysis are carried out by the on-chip UMZIs. The energy-time entangled photons are detected by single photon detectors. AWG: arrayed waveguide grating; UMZI: unbalanced Mach-Zander interferometer

1-kilomiter-long fibers, the high quantum interference visibility is achieved and proves the effectiveness of the multi-chip system. The system will play an important role in dense quantum communication and building up practical quantum networks.

Results

Details of the photonic chips

The quantum photon-pair source serves as the sender. It includes one SOI helical waveguide with a cross section of $220\,\text{nm} \times 500\,\text{nm}$. Wideband correlated photons are generated via the spontaneous four-wave mixing (SFWM) process in the waveguide [38]. The HIDS chips serve as the receivers. The 1×32 AWG, 32 balanced MZIs and 32 UMZIs are integrated on a single chip (shown in Fig. 2(a)). The waveguide has a cross-section of $2 \times 2\,\mu\text{m}$ to support single mode propagation. The waveguide transmission loss is very low, $\sim 0.05\,\text{dB/cm}$, which is ideal for on-chip long-time delay. Two arms of the UMZI have a relative time delay of $400\,\text{ps}$ (unbalanced length is $\sim 7.38\,\text{cm}$, which introduce an extra loss of $\sim 0.37\,\text{dB}$), which is used to distinguish the photon coincidence counting peaks. A balanced MZI is employed in the short arm of the UMZI for energy compensation through modulation of the on-chip platinum micro-heater (not shown in Fig. 1(a)). The phase differences of the two arms of UMZIs are tuned using micro-heaters covering the delay spiral waveguides. The size of the on-chip integrated 1×32 AWG is $6.2\,\text{mm} \times 8.0\,\text{mm}$ (Fig. 2(b)). The 3-dB passband width of the AWG channel is approximately $0.3\,\text{nm}$, and the insert loss variation is less than $4\,\text{dB}$ for all channels. The crosstalk among all channels is less than $-30\,\text{dB}$. The wavelength and channel spacing of the AWG meet the standard international telecommunications union (ITU) grids. All the input and output waveguides are arranged in a column with a pitch of $127\,\mu\text{m}$ coupled by a 128-channel fiber array. The coupling loss is less than $1.5\,\text{dB/facet}$. We select 17 channels, and their transmission spectra are shown in Fig. 2(d).

Entanglement distribution of one sender and one receiver

Firstly, we distribute the multi-wavelength correlated photons to one receiver chip. As shown in Fig. 3(a), a continuous-wave laser (TSL-550, Santec) centered at $1537.40\,\text{nm}$ (center of the C50 channel of ITU grids) is used as the pump ($23\,\text{mW}$ off chip) to generate photon pairs through the SFWM process in an SOI waveguide on Chip I. We use one PC before chip I to vary the polarization of the pump to guarantee maximum photon-pair generation. A prefilter of $100\,\text{GHz}$ is utilized to eliminate noise, mainly the broadband background fluorescence of the amplified spontaneous emission effect in the pump laser. A post filter of $200\,\text{GHz}$ is used to reject the residual pump and protect the single photon detectors. Both filters exceed $100\,\text{dB}$ isolation. After narrowing the bandwidth with one bandpass filter, the generated photon pairs are injected into Chip II, which is composed of an AWG and UMZIs. We use this chip for the energy-time entanglement preparation and analysis. The polarization of photons injected into Chip II is also fixed by another PC (not shown) to ensure TE_0 mode excitation.

The AWG serves as a critical DWDM component. It has 32 output ports, as shown in Fig. 2(b). We select 17 of them to demonstrate the entanglement distribution experiment (transmission spectra shown in Fig. 1(d)) and label them as CH1 to CH17 by wavelength from long to short. Their functionalities and the correspondence with standard DWDM
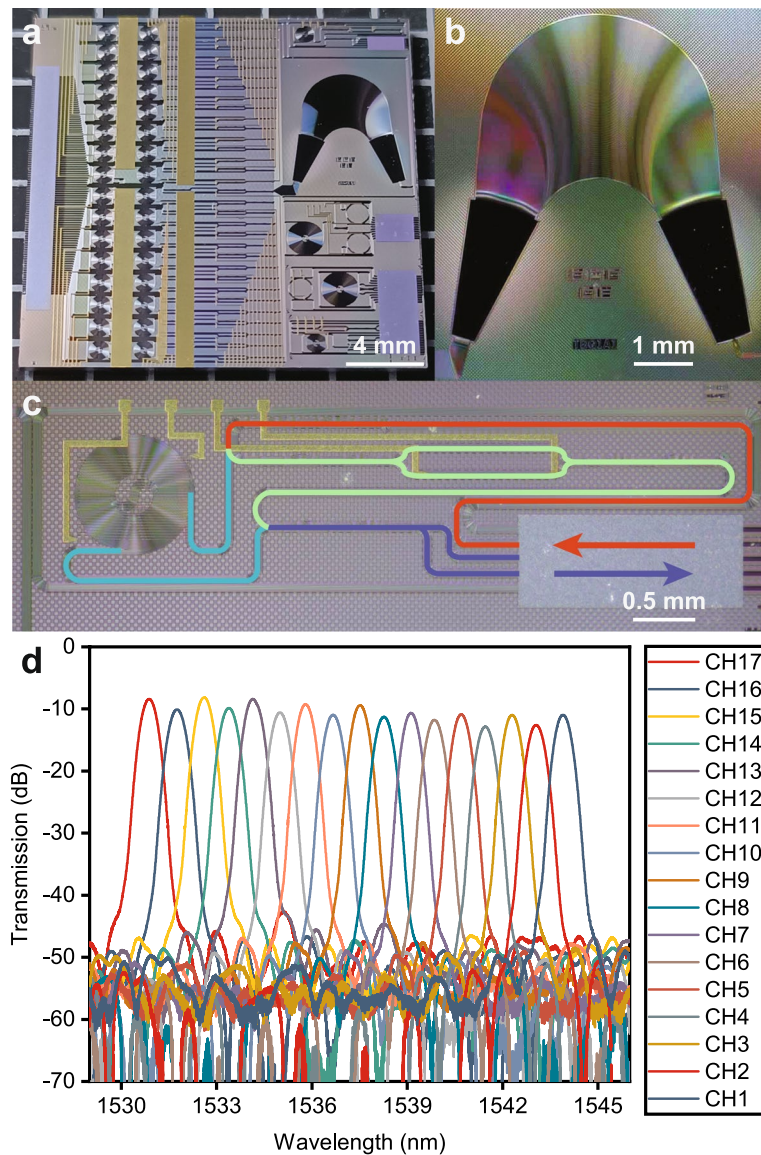
Fig. 2 Characterization of the samples. **a** A CCD photograph of the energy-time entanglement preparation chip, composed of a 32-channel AWG, 32 balanced MZIs and 32 UMZIs, 64 on-chip heaters, coupled with a 128-channel fiber array. **b-c** Microscope images of the AWG and UMZI. **d** Transmission of the 17 selected channels of the AWG, centered at C50 of international telecommunications union (ITU) grids

channels are given in Table 1. The output photon pairs are detected by superconducting nanowire single-photon detectors (SNSPDs, Scontel) with time jitter 45 ps. The generated electric signals are imported into the time-correlated single photon counting (TCSPC) system for the correlation analysis.

In the experiment, the spiral on Chip II provides a time delay (ΔT) of 400 ps, which meets the condition for energy-time entanglement generation. That is, $\tau_2 \ll \Delta T \ll \tau_1$, where τ_2 is the coherence time of the single photons (~ 25 ps, which is estimated by the reciprocal of the photon bandwidth) and τ_1 is the coherence time of the continuous pump laser [39]. The photonic state after the AWG and UMZIs can be described as $\frac{(e^{i\varphi_i}|L\rangle_i + |S\rangle_i)}{\sqrt{2}}$ and $\frac{(e^{i\varphi_s}|L\rangle_s + |S\rangle_s)}{\sqrt{2}}$, where ϕ_i and ϕ_s are the phase differences introduced by
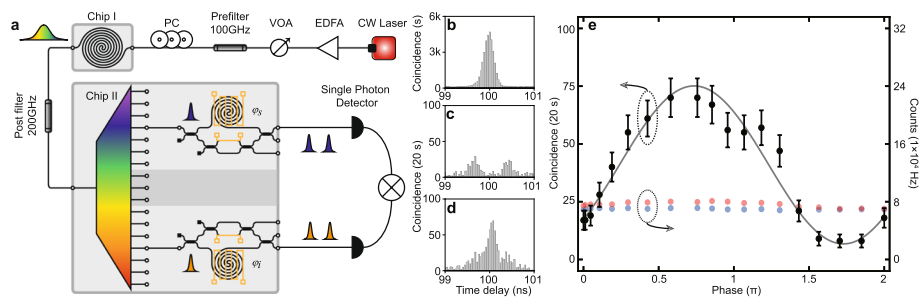
Fig. 3 Experimental setup and results for multi-channel entanglement distribution of one sender and one receiver. **a** Experimental setup. A silicon-on-insulator waveguide on Chip I serves as a quantum source. Chip II is the energy-time entanglement preparation and analysis chip. **b-c** Typical histograms of the interference peaks for CH11&CH7 of the AWG. The time resolution of the histograms is 40 ps. **d** The raw coincidence of the central peak for i_1-s_1 changes with phase. The black dots are measured coincidences. The gray curve is obtained by fitting the measured results using the sine function. The error bar comes from the Poisson statistical distribution. Red and blue dots refer to single channel counts of idler and signal photons, respectively. PC: polarization controller; VOA: variable optical attenuator; EDFA: erbium-doped fiber amplifier

Table 1 Definition and quantum interference visibilities of the AWG channel pairs. "s" and "i" represent "signal" and "idler" photons, respectively. It should be noted that the central three channels (CH8, CH9 and CH10) of the AWG are in the range of the post filter (gray zone in Chip II in Fig. 3(a)). Thus, their visibilities are absent

AWG channels	ITU channels	Functionality	Raw Visibility
CH17&CH1	C58&C42	s_7&i_7	92.008 ± 1.836%
CH16&CH2	C57&C43	s_6&i_6	96.179 ± 1.576%
CH15&CH3	C56&C44	s_5&i_5	93.423 ± 1.648%
CH14&CH4	C55&C45	s_4&i_4	96.329 ± 0.760%
CH13&CH5	C54&C46	s_3&i_3	95.047 ± 1.828%
CH12&CH6	C53&C47	s_2&i_2	91.035 ± 1.370%
CH11&CH7	C52&C48	s_1&i_1	91.007 ± 1.858%
CH10&CH8	C51&C49	–	–
CH9	C50	Pump	–

UMZIs for the idler and signal photons, and "L" and "S" represent the "Long" and "Short" time bins, respectively. The two-photon state is the direct product of single-photon states, which has the form of

$$\frac{1}{\sqrt{2}}\left(e^{i\varphi_i}|L\rangle_i + |S\rangle_i\right) \otimes \frac{1}{\sqrt{2}}\left(e^{i\varphi_s}|L\rangle_s + |S\rangle_s\right) = \frac{1}{2}\left(e^{i(\varphi_i+\varphi_s)}|L\rangle_i|L\rangle_s + e^{i\varphi_i}|L\rangle_i|S\rangle_s + e^{i\varphi_s}|S\rangle_i|L\rangle_s + |S\rangle_i|S\rangle_s\right),$$

and will be recognized by the TCSPC system as three coincidence peaks separated by "ΔT" (see Fig. 3(b-c)). The central peak (a time delay of 0) indicates the energy-time entanglement state, which has the form of

$$|\varphi\rangle = \frac{1}{\sqrt{2}}\left(e^{i(\varphi_i+\varphi_s)}|L\rangle_i|L\rangle_s + |S\rangle_i|S\rangle_s\right).$$

The central peak coincidence C is proportional to $(1+V\cos(\phi_i+\phi_s))$, where V is the visibility of the coincidence curve. By tuning the phases $\phi_i+\phi_s$ with on-chip heaters, we test every correlated channel pair and list their quantum interference visibilities in Table 1. All raw visibilities are over 90%, which proves that the integrated circuits have
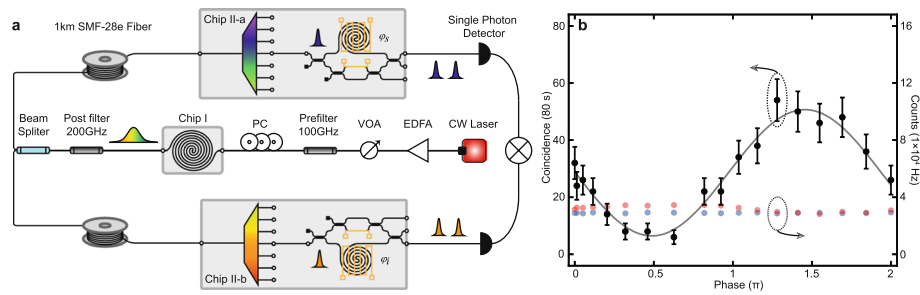
Fig. 4 Experimental setup of multi-channel entanglement distribution of one sender and two receivers. **a** Experimental setup. A silicon-on-insulator waveguide on Chip I serves as a quantum source. Chip II-a and Chip II-b are energy-time entanglement preparation and analysis chips, which serve as the receivers. Standard single mode fibers with one-kilometer length connect the chips **b** The raw coincidence of the central peak for CH11&CH7 versus phase. The black dots are measured coincidences. The gray curve is obtained by fitting the measured results using the sine function. The error bar comes from the Poisson statistical distribution. Red and blue dots refer to single channel counts of idler and signal photons, respectively

Table 2 Definition and quantum interference visibilities of the AWG channel pairs in the multi-chip entanglement distribution

AWG channels	ITU channels	Functionality	Raw Visibility
CH17&CH1	C58&C42	s_7&i_7	85.088 ± 2.456%
CH14&CH4	C55&C45	s_4&i_4	87.646 ± 2.203%
CH11&CH7	C52&C48	s_1&i_1	87.235 ± 1.815%

high quality and are ready for further quantum information applications. The typical coincidence curve of CH11&CH7 (C52&C48 of ITU) and their single channel counts as a function of phase on the long arm of UMZI are shown in Fig. 3(d). Coincidence curves for other channels can be found in the Supplementary Materials.

Entanglement distribution of one sender and two receivers

The results of the former experiment prove that our chips work well in generating and analyzing energy-time entanglement. Furthermore, we verify the feasibility of the chips for entangled distribution among three chips. In this part, we add another receiver chip (see Fig. 4 (a)). The photons generated by the SOI waveguide are divided by one BS and then sent to two receiver chips, namely, Chip II-a and Chip II-b for energy-time entanglement analysis. Two 1-km-long standard SMF-28e fibers connect the BS with the following two chips. We selected three equally spaced channel pairs and measured their coincidence versus phase. The quantum interference visibilities are listed in Table 2. All the raw visibilities are over 85%.

Discussion

In the experiment, the arm length difference of the UMZIs is 400 ps, which is mainly limited by the detectors' time jitter and coherence time of the single photons. Using a temporally narrowband light source and smaller time jitter detectors, we are able to decrease the arm length difference, which facilitates further construction of high-dimensional energy-time entanglement on the single chip. Due to the ultralow transmission

loss of the HIDS waveguide, long time delay UMZIs can be easily achieved. On the basis of our structure, a multi-wavelength high-dimensional energy-time entanglement distribution can be demonstrated by the cascade of UMZIs, thereby further increasing the system capacity. With another on-chip UMZI to modulate the pulsed pump laser, our scheme can be easily extended to another commonly used scheme, the time-bin entanglement distribution [40]. Because multiple-wavelength channels of the receiver chips support simultaneous operations by different users and more nodes can be constructed with more similar integrated chips, our work advances the quantum technologies for large-scale and complex quantum networks.

Conclusions

This work first integrates DWDM components with UMZIs monolithically and demonstrates multi-chip entanglement distribution with high interference visibilities. Benefiting from the low loss, low optical nonlinearity and high integration density of the HIDS platform, this work is promising for extending to high-dimensional energy-time and time-bin entanglement distributions among multiple users. With many other integrated structures, more complex and larger quantum networks will be built.

Methods

Thermal control is critical to the experiment. The resistance of heaters on the short balance MZIs is $\sim 170\,\Omega$, which requires a current of $\sim 50\,$mA to adjust a 2π phase. The heaters on the spiral waveguide of UMZIs have resistance of $\sim 1.5\,$kΩ, and a current supply of $\sim 14\,$mA is enough to finish a coincidence curve measurement. In our experiment, a custom-made high-power current source is used. To stabilize the operation temperature during the experiment, the integrated chip is mounted on a thermoelectric cooler (TEC), which is driven using a TEC controller (TED200C, Thorlabs). Conductive silver glue is used to fill the contact surfaces (see Supplementary Materials). The temperature coefficient of the AWG central wavelength is $\sim 18\,$pm/°C, which can be utilized to align the central wavelength of the AWGs with the standard of ITU grids and ensure that the system works properly.

Abbreviations

BS	Beam splitter
PIC	Photonic integrated circuits
QPICs	Quantum photonic integrated circuits
DWDM	Dense wavelength-division multiplexing
WDM	Wavelength-division multiplexing
UMZI	Unbalanced Mach-Zehnder interferometer
QKD	Quantum key distribution
SiN	Silicon nitride
AWG	Arrayed waveguide grating
SOI	Silicon-on-insulator
LNOI	Lithium niobate on insulator
HIDS	High-index doped silica
MZI	Mach-Zehnder interferometer
CMOS	Complementary metal oxide semiconductor
SFWM	Spontaneous four-wave mixing
ITU	International telecommunications union
PC	Polarization controller
VOA	Variable optical attenuator
EDFA	Erbium-doped fiber amplifier
FSR	Free spectral range
TE	Transverse electric

SNSPD	Superconducting nanowire single-photon detectors
TCSPC	Time-correlated single photon counting
TEC	Thermoelectric cooler

Supplementary Information

The online version contains supplementary material available at https://doi.org/10.1186/s43074-023-00089-1.

Additional file 1: S0. Characterization of the quantum source. **Fig. S0.** Coincidence peak for $i_1\&s_1$. The resolution histogram is set to be 40 ps. **S1.** Coincidence curves for other channels in the experiment of dense energy-time interference. **Fig. S1.** The raw coincidences of the central peak versus phase from i_2-s_2 to i_7-s_7. **S2.** Coincidence curves for other channels in multichip entanglement distribution over 1-km standard fibers. **Fig. S2.** The raw coincidences of the central peak versus phase for i_4-s_4 and i_7-s_7. **S3.** The effect of the free spectral range (FSR) of arrayed waveguide gratings (AWGs) on coincidence. **Fig. S3.** Coincidence peaks with/without bandpass filters for $i_5\&s_5$. **S4.** Packaged chip with electric supply. **Fig. S4.** (a) Packaged and mounted chip ready for testing. (b) Fiber distribution box for 128-channel I/O. **S5.** The classical characterization of the on-chip balanced Mach-Zehnder interferometer (MZI) and unbalanced Mach-Zehnder interferometer (UMZI). **Fig. S5.** (a) The classical interference curve of the on-chip balanced MZI. **Fig. S5.** (b) The classical interference curve of the on-chip UMZI.

Availability of data and materials

Supplementary information is available in the online version of the paper.

Declarations

Ethics approval and consent to participate

There is no ethics issue for this paper.

Consent for publication

All authors agreed to publish this paper.

Competing interests

The authors declare that they have no competing interests.

References

1. Joshi SK, et al. A trusted node-free eight-user metropolitan quantum communication network. Sci Adv. 2020;6:eaba0959.
2. Fröhlich B, et al. A quantum access network. Nature. 2013;501:69–72.
3. Jayakumar H, et al. Time-bin entangled photons from a quantum dot. Nat Commun. 2014;5:4251.
4. Cuevas A, et al. Long-distance distribution of genuine energy-time entanglement. Nat Commun. 2013;4:2871.
5. Zhang M, et al. Electronically programmable photonic molecule. Nat Photonics. 2019;13:36–40.
6. Wang J, Sciarrino F, Laing A, Thompson MG. Integrated photonic quantum technologies. Nat Photonics. 2020;14:273–84.
7. Feng L, et al. Silicon photonic devices for scalable quantum information applications. Photonics Res. 2022;10:A135–53.
8. Feng L, et al. On-chip coherent conversion of photonic quantum entanglement between different degrees of freedom. Nat Commun. 2016;7:11985.
9. Ren S, et al. Single-photon nonreciprocity with an integrated magneto-optical isolator. Laser Photonics Rev. 2022;16:2100595.

10. Pelucchi E, et al. The potential and global outlook of integrated photonics for quantum technologies. Nat Rev Phys. 2022;4:194–208.
11. Harris NC, et al. Integrated source of spectrally filtered correlated photons for large-scale quantum photonic systems. Phys Rev X. 2014;4:41047.
12. Wang J, et al. Multidimensional quantum entanglement with large-scale integrated optics. Science. 2018;360:285–91.
13. Metcalf BJ, et al. Quantum teleportation on a photonic chip. Nat Photonics. 2014;8:770–4.
14. Broome MA, et al. Photonic boson sampling in a tunable circuit. Science. 2013;339:794–8.
15. Paesani S, et al. Generation and sampling of quantum states of light in a silicon chip. Nat Phys. 2019;15:925–9.
16. Politi A, Matthews JCF, O'Brien JL. Shor's quantum factoring algorithm on a photonic chip. Science. 2009;325:1221.
17. Santagati R, et al. Witnessing eigenstates for quantum simulation of Hamiltonian spectra. Sci Adv. 2018;4:p9646.
18. Zhang Z, et al. High-performance quantum entanglement generation via cascaded second-order nonlinear processes. npj Quantum Inf. 2021;7:123.
19. Xu B, et al. Spectrally multiplexed and bright entangled photon pairs in a lithium niobate microresonator. Sci China Phys Mech. 2022;65:294262.
20. Feng L, Guo G, Ren X. Progress on integrated quantum photonic sources with silicon. Adv Quantum Technol. 2020;3:1900058.
21. Li Y, et al. On-chip multiplexed multiple entanglement sources in a single silicon nanowire. Phys Rev Appl. 2017;7:64005.
22. Wengerowsky S, et al. An entanglement-based wavelength-multiplexed quantum communication network. Nature. 2018;564:225.
23. Williams BP, et al. Reconfigurable quantum local area network over deployed fiber. PRX Quantum. 2021;2:40304.
24. Aktas D, et al. Entanglement distribution over 150 km in wavelength division multiplexed channels for quantum cryptography. Laser Photonics Rev. 2016;10:451–7.
25. Dong S, et al. Energy-time entanglement generation in optical fibers under CW pumping. Opt Express. 2014;22:359–68.
26. Liu X, et al. 40-user fully connected entanglement-based quantum key distribution network without trusted node. PhotoniX. 2022;3:2.
27. Xiong C, et al. Compact and reconfigurable silicon nitride time-bin entanglement circuit. Optica. 2015;2:724.
28. Zhang X, et al. Integrated silicon nitride time-bin entanglement circuits. Opt Lett. 2018;43:3469–72.
29. Pathak S, Dumon P, Van Thourhout D, Bogaerts W. Comparison of AWGs and echelle gratings for wavelength division multiplexing on silicon-on-insulator. IEEE Photonics J. 2014;6:1–9.
30. Sugita A, et al. Very low insertion loss arrayed-waveguide grating with vertically tapered waveguides. IEEE Photonic Tech L. 2000;12:1180–2.
31. Nishi H, et al. Monolithic integration of a silica AWG and Ge photodiodes on Si photonic platform for one-chip WDM receiver. Opt Express. 2012;20:9312–21.
32. Wang J, et al. Low-loss and low-crosstalk 8 × 8 silicon nanowire AWG routers fabricated with CMOS technology. Opt Express. 2014;22:9395–403.
33. Bogaerts W, et al. A polarization-diversity wavelength duplexer circuit in silicon-on-insulator photonic wires. Opt Express. 2007;15:1567–78.
34. Bogaerts W, et al. Silicon-on-insulator spectral filters fabricated with CMOS technology. IEEE J Sel Top Quant. 2010;16:33–44.
35. Piels M. Low-loss silicon nitride AWG demultiplexer heterogeneously integrated with hybrid III–V/silicon photodetectors. J Lightwave Technol. 2014;32:817–23.
36. Li J, et al. AWG optical filter with tunable central wavelength and bandwidth based on LNOI and electro-optic effect. Opt Commun. 2020;454:124445.
37. Xu Y, Lin H. A concise design of 16×16 polymer AWG with low insertion loss and crosstalk. Optik. 2014;125:920–3.
38. Zhang M, et al. Generation of multiphoton quantum states on silicon. Light Sci Appl. 2019;8:41.
39. Franson JD. Bell inequality for position and time. Phys Rev Lett. 1989;62:2205.
40. Brendel J, Gisin N, Tittel W, Zbinden H. Pulsed energy-time entangled twin-photon source for quantum communication. Phys Rev Lett. 2001;86:1392.

Publisher's Note